Acta Astronautica 242 (2026) 74–84

Contents lists available at ScienceDirect

Acta Astronautica

journal homepage: www.elsevier.com/locate/actaastro

Research Paper

Airborne re-entry observation campaign of the Cluster-II salsa re-entry

Stefan Loehle [a,*], Fabian Zander [b], Patrik Kaerraeng [c], Tobias Lips [c], Gerard Armstrong [b], Byrenn Birch [b], Ranjith Ravichandran [b], Clemens Mueller [a], Juraj Toth [d], Tomasz Paulech [d], Jiri Silha [d], Matej Zigo [e], Beatriz Jilete [f], Stijn Lemmens [e]

[a] High Enthalpy Flow Diagnostics Group, Institute of Space Systems, University of Stuttgart, Pfaffenwaldring 29, Stuttgart, 70569, Germany
[b] University of Southern Queensland, 487-535 West St, Darling Heights, QLD 4350, Australia
[c] Hypersonic Technology Goettingen, Am Handweisergraben 13, Bovenden, 37120, Germany
[d] Comenius University of Bratislava, Safarikovo Namestie 6, Bratislava, 81499, Slovakia
[e] Astros Solutions s.r.o., Ilkovicova 8, Bratislava, 84104, Slovakia
[f] European Space Agency, Robert-Bosch-Strasse 5, Darmstadt, 64293, Germany

ARTICLE INFO

Keywords:
Re-entry
Airborne Observation
Cluster Satellite

ABSTRACT

After their end of operation, the four Cluster-II satellites are re-entering the Earth's atmosphere. The first Cluster-II satellite, named *Salsa*, re-entered on the 8th of September at 18:46 UTC (2024-09-08T18:46 UTC) over the South Pacific, approximately 2000 km west of Easter Island. An airborne observation team was on station aiming to observe the satellite's break-up. This paper reports the design and execution of the airborne observation under the challenging situation of an entry under plain daylight conditions. The mission planning and preparation in coordination with the observation prediction leads to the flight mission details. Due to the highly eccentric orbit, the entry predictions were particularly challenging and resulted in a wider spread of potential entry corridors. Therefore, based on the very last perigee, only 52 h before the actual entry, and spacecraft data after the maneuver, the team received the last orbit information at 20:30 UTC on the 7th of September (2024-09-07T20:30UTC). Based on this data an appropriate flight path for the aircraft was designed. On board a Falcon 900 business jet, the team deployed six different stations with a total of 26 cameras. All cameras were time-synchronized to the GPS time using a centralized time server. The mission was successful. The infrared cameras detected the entry for approximately 23 s beginning at around 18:47:08 UTC.

1. Introduction

The rapidly growing number of satellites in orbit generates the continuously increasing risk of space debris impacting on ground when a satellite enters the Earth's atmosphere. Most recently, a battery pack from the International Space Station showed dramatically what might happen if the re-entry break-up does not result in a full demise of the spacecraft.[1] At the time of writing, a 500 kg *fragment of a space object* has just been reported as landing on Mukuku, a small, remote village in Kenya,[2] providing another pertinent example of the danger caused by space debris.

The European Space Agency (ESA) strives to advance the European effort to minimize the causality risk. Under the Clean Space Initiative and Design for Demise umbrella, new satellites are designed to have a high probability for a full demise during the re-entry process or perform controlled re-entries. In the case of Cluster-II, also novel ways of targeting re-entries for rarer orbit types are operationally tested [1–3].

The first European re-supply spacecraft to the International Space Station (ISS) named the *Automated Transfer Vehicle (ATV-1)* was successfully observed in 2008 [4,5]. The last ATV, ATV-5, was also targeted for observation, but the observation mission had to be canceled due to power issues aboard the spacecraft resulting in an earlier-than-planned re-entry [6]. In 2015, an unknown object named WT1190F returned to Earth. An airborne observation campaign was developed within only 4 weeks after the object was first detected and was successfully executed [7]. Based in part on the observation data it has been concluded that the object was a Lunar Insertion Stage from 1998 [8]. In 2016, the re-supply spacecraft *CYGNUS-OA6* to the ISS developed by Orbital ATK was observed, again from an aircraft over the South Pacific Ocean attempting to provide data about the break-up of the spacecraft

* Corresponding author.
E-mail address: loehle@irs.uni-stuttgart.de (S. Loehle).

[1] https://www.universetoday.com/166681/nasa-confirms-that-a-piece-of-its-battery-pack-smashed-into-a-florida-home/
[2] https://edition.cnn.com/2025/01/02/science/kenya-space-object-intl-latam

https://doi.org/10.1016/j.actaastro.2026.01.030
Received 17 March 2025; Received in revised form 26 November 2025; Accepted 13 January 2026
Available online 14 January 2026

to the modeling community [9]. A similar *CYGNUS-NG20* spacecraft was observed very recently in July 2024 by the University of Southern Queensland, the University of Kentucky and HEFDiG.

Besides these destructive re-entries, there have been several observations of re-entering objects with a targeted landing on ground. It started with the Genesis capsule, followed by the observation of the Stardust capsule [10,11], both NASA missions. In 2010 and 2020, the two Hayabusa capsule re-entries were observed [12–14] and most recently, the entry of OSIRIS-REx was observed by four aircraft in September 2023, again with participation from the University of Southern Queensland and HEFDiG.

However, there is still a significant lack of flight data on destructive re-entries which can be used to validate the prediction tools. The Cluster satellites are ideal candidates to close some gaps. There are four of them and the entries are separated by about one year, the last two which enter within 24 h period. This allows the observation of the same object under different conditions and with respect to the observation campaign itself, each campaign can be improved from the lessons learned during the previous one.

The Cluster-II *Salsa* observation mission was agreed on early in 2024 and during the preparation phase, three main objectives have been condensed. All destructive re-entries have a main break-up event typically occurring in an altitude range between 80 km and 70 km, most LEO entries' main break-up occurs at an altitude of 78 km. Recent ground testing indicates that this main break-up at 78 km is not a coincidence [15]. The observation of the re-entry of a known object therefore is an ideal candidate to gain more insight into the break-up phenomena. Furthermore, the Cluster-II enters at a very high velocity of 11 km/s, so a satellite structure on a different entry trajectory than the above-mentioned already observed objects.

Besides the detection of the main break-up event, the number of fragments developing after the explosion is of particular importance to validate the modeling tools. Here, using instruments with a longer focal length can help observing a smaller field of view and therefore allow to see the fragments in more detail. However, a longer focal length comes at the cost of a higher risk of losing the target during manual tracking.

The third objective of the observation of this re-entry is to identify fragments by measuring their spectral features. However, since it is a daytime entry, spectroscopic setups using transmission gratings as it is typically applied in re-entry observations are very challenging and in the visible wavelength interval probably not feasible. A transmission grating would suffer from the fact that next to the spectra of a feature of interest, the blue sky overlays the same sensor area, i.e. the sensor is quickly saturated by background or the event has to be extremely bright so that the signal arises on top of the noise. For the present observation, a number of filtered imaging cameras and three transmission gratings options behind long pass filters in the near IR wavelength interval, were used to overcome the background.

The next sections present the approach to predict the re-entry, the flight path definition for the aircraft, a description of the onboard sensor system and finally some first results.

2. Pre-flight predictions

A fundamental requirement for the execution of a mission is to know exactly where the object will enter the Earth's atmosphere and based on this prediction an appropriate flight path for the aircraft has to be designed. For the entry prediction, the starting point requires to know where the spacecraft will be on its last orbit. The next subsection provides more details on this. The aircraft flight path has some further restrictions with respect to air traffic control and safety requirements for the distance between aircraft and entering object. Details are given in Section 2.2.

2.1. Re-entry prediction

Hypersonic Technology Goettingen (HTG) is performing predictions of re-entry break-up using their in-house developed software *(Spacecraft Atmospheric Re-enty and Aerothermal Break-up, SCARAB)* [16]. The software calculates the destructive re-entry with occurring fragmentation and predicts the eventual probability of fragments hitting ground.

The software's main input is the detailed spacecraft structure and the orbital condition of the spacecraft, usually given by orbital telemetry data. For the re-entry prediction, SCARAB requires at minimum the entry state and a ballistic coefficient to start with [16]. The whole spacecraft is modeled starting with simple area elements combined to substructures which eventually integrate up to the whole satellite. Each structure requires a material, center of mass and mass definition. For the material selection, SCARAB provides a number of materials with temperature-dependent thermo-physical properties. A typical re-entry passes three different regimes of aerodynamics: the free-molecular flow, continuum hypersonic flow and super- to subsonic flow. The main break-up at altitudes below 80 km occurs under continuum fluid flow. Here, the theory of Lees is applied to determine the aerothermodynamic heating in the hypersonic, continuum flow regime [17]. Thus, heating is mainly driven by the inclination of the respective surface element with respect to the flight direction.

In the present case the entry situation was dictated by the orbital situation, i.e. no distinct de-orbit maneuver was triggered. During the last perigee pass the satellite was already decelerated significantly by the atmosphere. Thus, the uncertainty of where exactly the entry would happen is high until the last orbit when the situation becomes fully known. Fig. 1 shows the arrival uncertainty as known on 12 August 2024, i.e. about one month before entry. As can be seen there is a significant difference. The distance in between two options results to more than 2000 km. Assuming an aircraft speed of 800 km/h, the entry location cannot be changed on the spot. Thus, this prediction fundamentally affects the re-entry observation. Therefore an automatic communication protocol was setup, in order to receive the predictions automatically until the very last possibility. The last perigee traverse was about 52 h before re-entry.

The re-entry predictions calculated by HTG were based on the state vectors at a 130–120 km altitude range determined from spacecraft telemetry and observations provided by a network of telescopes. The inputs required by HTG, were the outcome of a coordination effort between different groups in ESA. Telemetry data reception was coordinated by the Cluster Flight Control Team. This telemetry was used by the Cluster Flight Dynamics Team to perform orbit determination and estimate the drag coefficient upon. An international collaboration observation campaign was established via the IADC, where several sensors provided regular observations. To highlight some of them: ESA OGS telescope operated by ESA Planetary Defence team, Zimmerwald observatory, AGO70 telescope, State Space Agency of Ukraine (SSAU) sensors. ESA Space Debris Office was in charge of the computation of the state vectors by combining the information from Flight Dynamics Team and sensor observations.

Eventually, the re-entry break-up is calculated by HTG upon new telemetry data is arriving on the server. The calculation itself, including conservative margins, takes 2.5 hours. The result is then communicated to the mission team, so that the aircraft's flight path can be designed using these data. This takes another hour. For safety reasons, a short message system has been setup, providing main entry times and locations in a 160 character message, just in case internet connection in South Pacific is insufficient.

Fig. 2 shows the re-entry fragmentation prediction output from SCARAB as altitude versus UTC time. The red curve is the center of the fragment cloud, which for the beginning of the entry corresponds to the entire spacecraft still being intact. The break-up starts at 18:47:00 UTC according to this prediction.

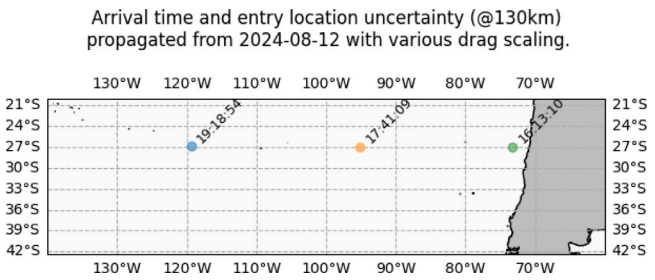

Fig. 1. Re-entry break-up prediction: uncertainty of the re-entry location based on trajectory data from 2024-08-12.

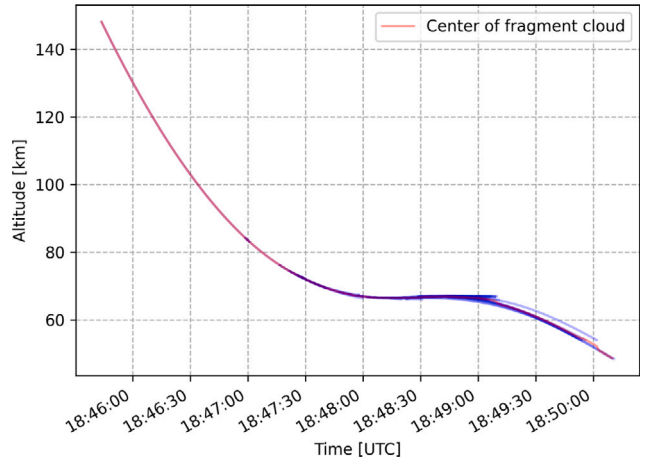

Fig. 2. Scarab re-entry break-up prediction: fragment's altitude with time.

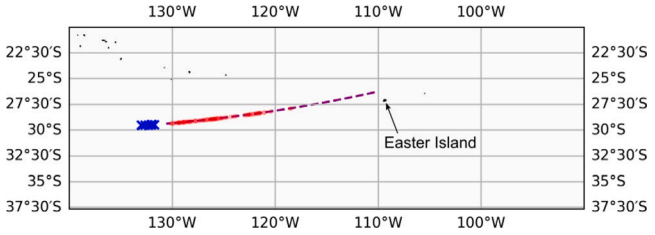

Fig. 3. Re-entry location and ground impact prediction.

Fig. 3 shows the entry location and the fragments that will survive the entry and hit the ocean. The SCARAB simulation predicts that the 6 fuel tanks will eventually impact the ocean. Fig. 4 shows the number of fragments to be seen at a certain instant in time. This representation is used to sketch a target point for the positioning of the aircraft. The focus is considered to be the first significant break-up assumed to be visible as a flare. It is the event at 18:47:30 UTC, the green line in Fig. 4. As will be seen in the results section, the observed part of the entry was at the very first significant fragment development at 18:47:10 UTC.

The flight path of the aircraft is determined from this data, which is further detailed in the next section.

2.2. Flight path planning

The spacecraft enters the atmosphere with an initial velocity of 11.2 km/s. The aircraft's true flight speed is around 800 km/h. This means, there is a natural limit of how well the aircraft can *follow* the spacecraft. By flying a turn with the aircraft during the actual observation, the entering object remains in view for a longer duration. The location of the turn then determines which part of the trajectory is observed. If the aircraft is positioned further down with respect to the predicted trajectory, the beginning of the entry is not detectable. If the aircraft is positioned higher up with respect to the predicted trajectory, the fragmentation occurring later will become out of sight. The size of the windows and the resulting turning angle of the instrument limit the duration in which the spacecraft is visible.

As there are several lenses per window station, the possible camera azimuth capability is further reduced. Finally, the field of view (FOV) of the cameras is a further variable to be considered.

The determination of the flight path is thus a result of the requirement to answer a research objective, the limits in flight range and the possible positioning, flight maneuver options of the aircraft itself, and the possible view angles to be realized for the instrument setups at the aircraft window.

By setting a flight path of the aircraft, the angles between the predicted trajectory of the entering spacecraft and the aircraft can be calculated, which then allows the determination of the distance between the aircraft and the re-entry trajectory depending on time. When these angles are known, the view angles of a camera out of the window are calculated and finally, the FOV of a camera is added.

Fig. 5 shows the resulting flight path of the aircraft designed for this mission including spacecraft altitudes. Fig. 6 shows how the instrument has to be directed during flight, so elevation and azimuth in this plot are based on the aircraft's orientation. The window stations 1 – 4 are equipped with attitude acquisition. The rotation motion for azimuth and elevation in the tripod head is measured and recorded time synchronized with the GPS server during the observation flight. The colored dots indicate the altitude of the spacecraft at this pointing and the numbers are the distance of the object to the aircraft at this point.

The beginning of the observation mission is marked by the beginning of the aircraft turn, which is under a bank angle of 15 °. This is seen as the vertical line at the beginning in Fig. 6. The full curve shows the required pointing angles for the cameras to track the predicted spacecraft trajectory. The speed at which the cameras have to follow this path is not constant. In the beginning, the object is rather flying towards the aircraft, while later in time it is more a fly-by requiring the cameras to be moved faster. The movement of the cameras at the different stations in order to follow the object was rehearsed prior to the entry to anticipate the camera moving procedure. One person announced the angles in time and the operator moved the camera accordingly by setting the attitude as it appears on the attitude measurement unit.

3. Airborne observation campaign

The airborne observation is deployed out of Sydney, Australia. A commercial business jet of type Falcon 900 is flying the instruments and the team from Sydney via Auckland and Tahiti to Easter Island. The transfer flights are used for camera setup and adjustment. During the last transfer flight, a test countdown exercise is performed. Fig. 7 shows the cabin layout with the 6 window stations. The first three stations are operated by UniSQ, station 4 by HEFDiG, and stations 5 and 6 by the Comenius University Bratislava (CUB).

Each station can be mounted in front of two to three different windows. The optimal window is selected based on the cabin layout, including seat and table arrangements. For each station, a supporting plate structure was provided by UniSQ. The height on that platform can be adjusted with supporting aluminum structures. An excellent last minute adaptation option was provided by UniSQ, who setup a 3D printer in the hangar.

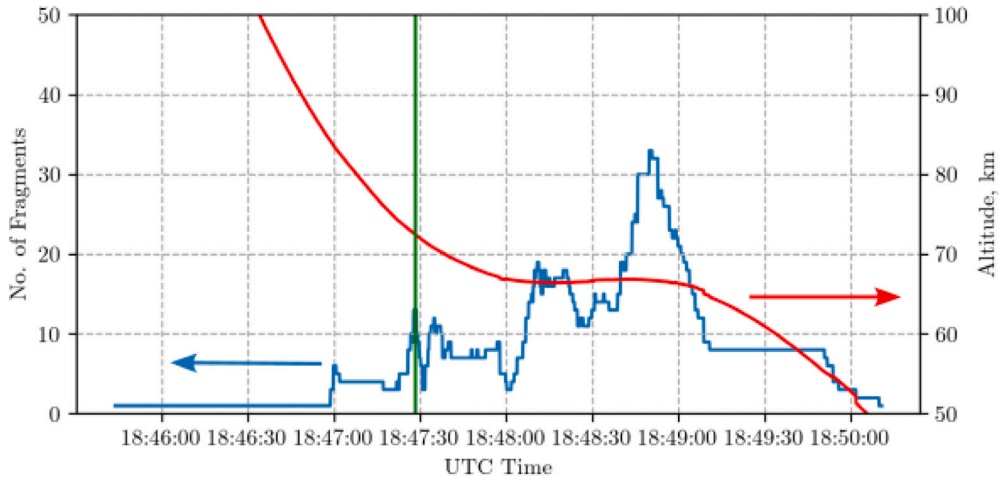

Fig. 4. Number of fragments developing during the time of observation.

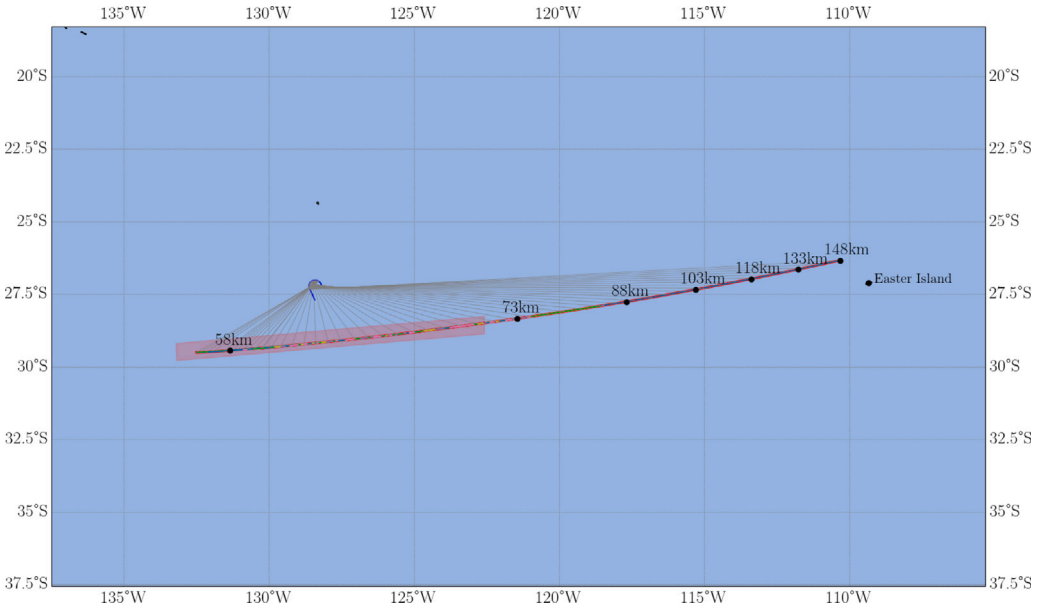

Fig. 5. Re-entering spacecraft flight path and aircraft positioning and flight path. Numbers indicate the altitude of the main fragment.

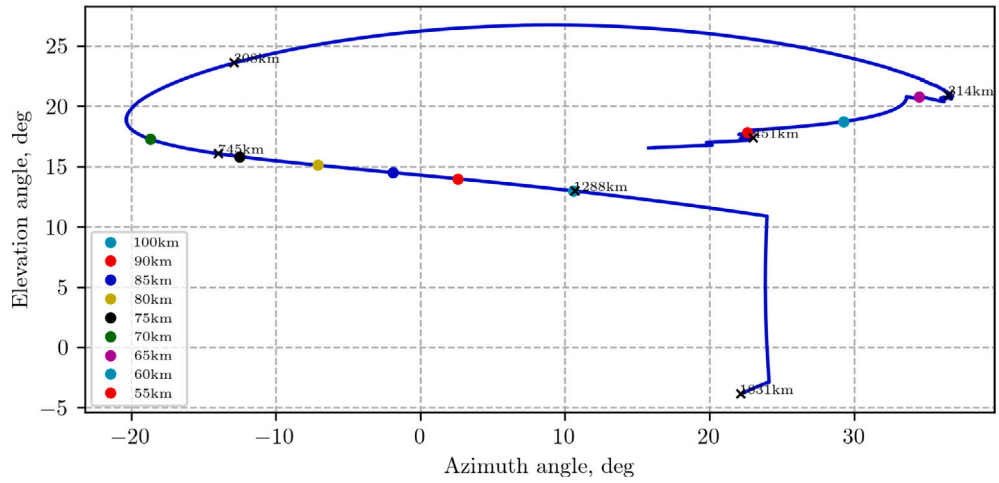

Fig. 6. Azimuth and Elevation of an instrument with respect to the aircraft.

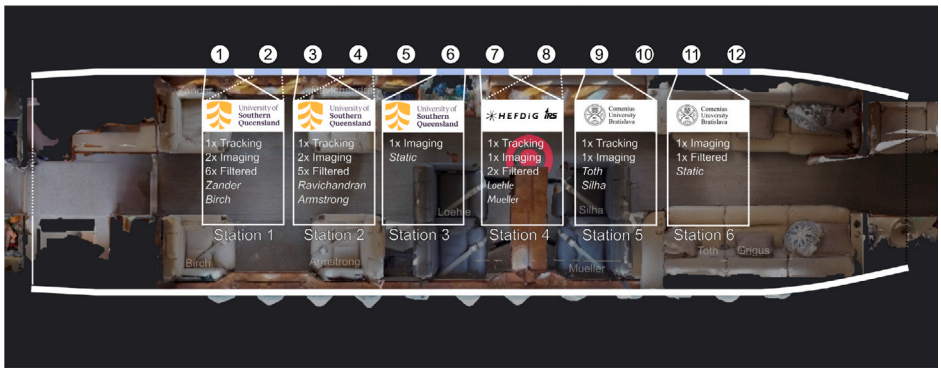

Fig. 7. Instrument and seating setup aboard the Falcon 900.

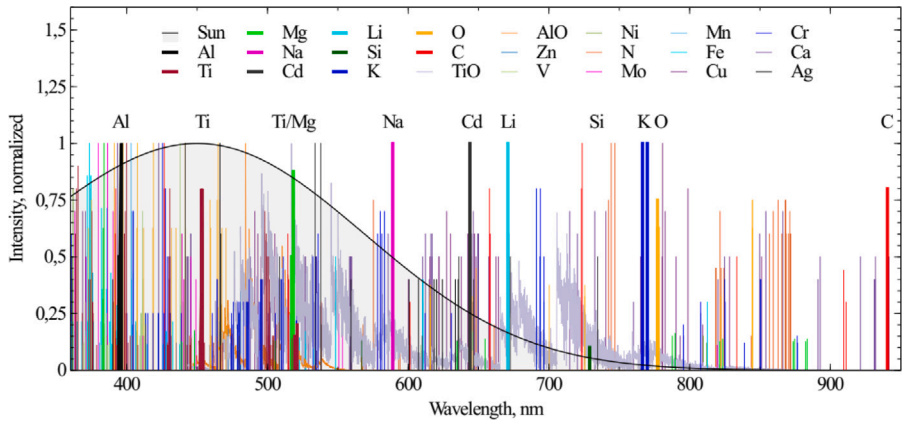

Fig. 8. Prominent emission lines of air plasma species and spacecraft materials.

3.1. Instruments

Since this observation mission is a daylight entry, the choice for sensors is very limited. The bright blue sky has to be blocked in order to separate the incoming capsule. So, long-pass filters are appropriate. However, this also means that the visible light is blocked, where strong atomic emission lines of metals are expected to be detectable.

The typically applied UV-NIR transmission grating spectroscopy is hardly applicable under these lighting conditions, particularly for the visible wavelengths. Due to the bright sunlight background, a system including a transmission grating would detect a spectra from neighboring sunlight and thus the camera is quickly saturated and the emission from the entering object becomes undetectable. Therefore, spectral differentiation is realized by using several cameras with appropriate spectral bandpass filters. Nevertheless transmission grating spectroscopy with additional longpass filtering has been seen as an option and was deployed as a test configuration. Fig. 8 shows prominent emission lines of air plasma species and spacecraft material's emission. Based on this plot, lines can be selected which are not affected significantly by another species within the bandpass filter's range. These lines are shown as bold lines in Fig. 8. The instruments are then – depending on their respective camera sensitivity – used with an appropriate filter. Furthermore, it needs to be checked that the different stations have a good distribution in order to realize a minimum of redundancy in case a station fails during the observation.

It was decided to try to detect mostly data expected from aluminum alloys, which account for more than half of the satellite's mass. Furthermore, silicon and titanium and carbon was considered. Sodium was added, because it always appears and could serve as an indicator for mission failure if no signal at all is measured. An indicator for the batteries is cadmium. Where possible lines at higher wavelengths were selected, so that the visible Rayleigh-scattered sunlight background effect is minimized. The elements to be detected are: Al (396 nm, 877 nm, 1312 nm), Ti (453 nm), Mg (520 nm), TiO (710 nm), Si (729 nm), C (940 nm), Li (670 nm), Na (589 nm), Cd (643 nm), K (770 nm). All bandpass filters have a full width at half maximum (FWHM) of 10 nm.

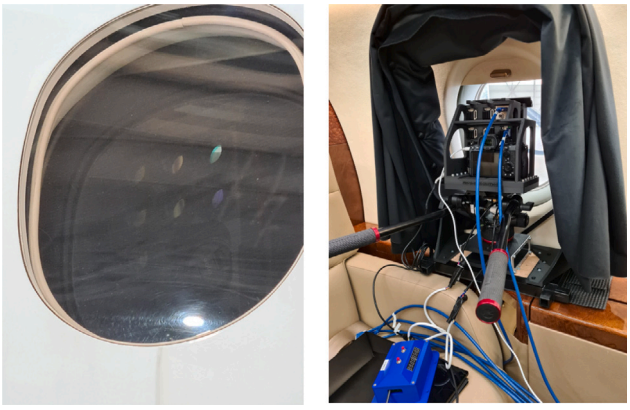

Fig. 9. Instrument setup at station 1: view from outside (left) and setup at window (right).

Table 1 shows a summary of the stations and mounted cameras. The last column indicates the purpose of the respective camera, either tracking (trk.), element detection (El.) or imaging (Img.) of the re-entry. Tracking cameras are mounted at each station, where an operator can change azimuth and elevation during the mission. The tracking camera assists the operator in spotting the object as it appears and enables

Fig. 10. Instrument setup at station 2.

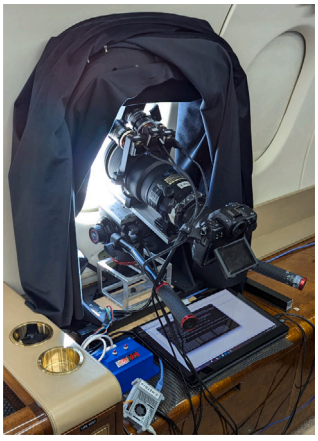

Fig. 11. Instrument setup at station 4.

Fig. 12. Instrument setup at station 5.

Fig. 13. Instrument setup at station 6.

Fig. 14. Instrument setup at the ground station.

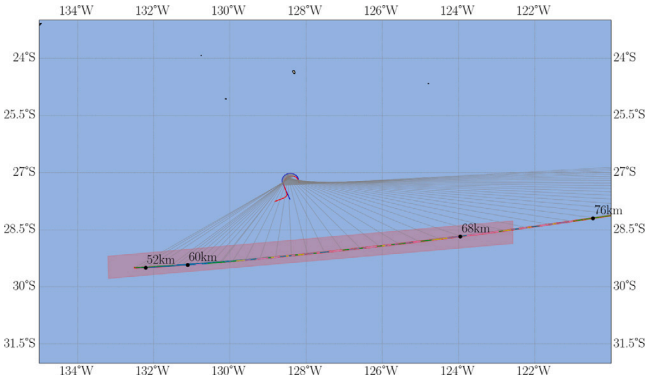

Fig. 15. Flown ground track overlaid on the pre-flight definition.

them to follow it. As mentioned in the previous section, the aircraft flight path is aligned to help the operators keep the re-entering object in the field of view. The different stations are described in the following sections.

3.2. Station 1

This station is equipped with 9 cameras. First, a Sony Alpha 7sIII with a $f = 50$ mm lens for pure imaging. Here, no additional filter is mounted. In total 7 Allied Vision Alvium 1800 cameras with different sensitivity options are used for filtered imaging and an additional Basler camera is mounted using a polarization imaging method recently developed at UniSQ. Fig. 9 shows the setup from outside through the aircraft window and from inside.

3.3. Station 2

This station is equipped with 8 cameras. Another Sony Alpha 7sIII with a $f = 50$ mm lens is used for imaging. Seven Allied Vision Alvium 1800 are deployed, two of them with short wave infrared (SWIR)

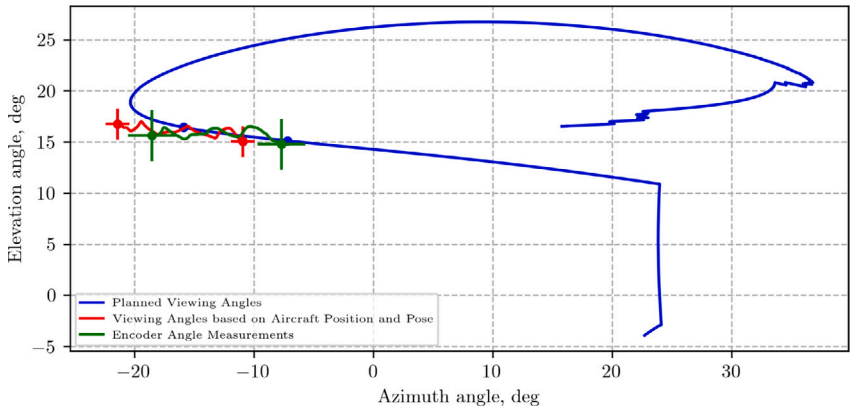

Fig. 16. Predicted track of the view out of the window in comparison with the real observation.

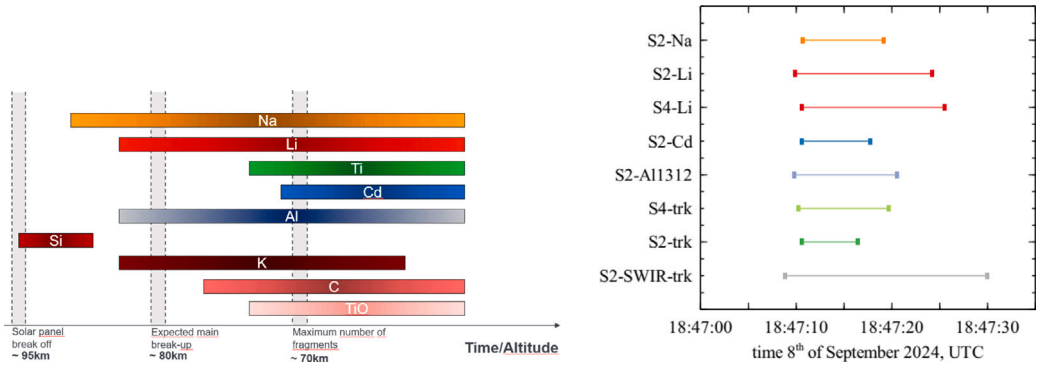

(a) pre-flight assumption (b) flight data

Fig. 17. Assumed species detection intervals (a) and actually detected species (b).

Table 1
Window stations with flown instrument/filter selection.

PI	Window	Camera	Lens	Filter	Idx
UniSQ	1	Sony a7sIII	50 mm lens	unfiltered	Img.
		Alvium 1800 U-812UV	25 mm UV	EO 394 nm filter - Al 396 nm	El.
		Alvium 1800 U-811M	16 mm	TL 520 nm filter - Ti/Mg 520 nm	El.
		Alvium 1800 U-811M	25 mm	TL 710 nm filter -TiO 710 nm	El.
		Alvium 1800 U-1242M	25 mm	TL 730 nm filter - Si 729 nm	El.
		Alvium 1800 U-507M	25 mm	777 nm - Atomic Oxygen	El.
		Alvium 1800 U-130 VSWIR	16 mm	TL FBH940-10 - C	El.
		Alvium 1800 U-508M	16 mm	650 nm long pass	Trk.
		Basler acA4112-30um-POL	35 mm	Polarization imaging	Img.
UniSQ	2	Sony a7sIII	50 mml	unfiltered	Img.
		Alvium 1800 U-811M	Fujinon 16 mm	TL 450 nm filter - Ti 453 nm	El.
		Alvium 1800 U-811M	25 mm	TL 670 nm filter - Li 671 nm	El.
		Alvium 1800 U-1242M	25 mm	TL 590 nm filter-Na 589 nm	El.
		Alvium 1800 U-811M	16 mm	TL 647 nm filter - Cd 643 nm	El.
		Alvium 1800 U-130 VSWIR	16 mm	TL 1310 nm filter - Al 1312 nm	El.
		Alvium 1800 U-130 VSWIR	16 mm	800/850 nm long pass	Img.
		Alvium 1800 U-508M	16 mm	650 nm long pass	Trk.
UniSQ	3	Sony a7sIII	30 mm	unfiltered	Img.
HEFDiG	4	NIKON Z8	300 mm	Longpass 645 nm	Img.
		Allied Vision 1800 U-501 m NIR, 300–1000 nm	16mm	Grating 300l/mm + Longpass 630 nm	El.
		Allied Vision 1800 U-811 m, 300–900 nm	25 mm	Longpass 630 nm	Trk.
		Allied Vision 1800 U-811 m, 300–900 nm	25 mm	TL FBH670-10 - Li	E.
Comenius	5	Mirror Less Nikon Z6 II	50 mm	77 mm polarization+longpass 500 nm	Img.
		Alvium 1800 U-130 VSWIR C-Mount	12 mm	500l/mm grating	El.
Comenius	6	Allied Vision 1800 U-2460 m	12 mm	longpass+500l/mm grating	El.
		DMK 33UX183 20 MP	16 mm	M55 K filter 770 nm	El.
Comenius	Grd.St.	Mirror Less Panasonic Lumix DC-S5IIX	50 mm	polarization+longpass 670 nm	Img.
		Sony Alpha 7III (IR, 360–1300 nm)	28 mm	unfiltered	Img.

sensitivity up to 1700 nm. One of these cameras is used for imaging, the second is used to detect aluminum at 1312 nm and is therefore equipped with the appropriate bandpass filter. The other Alviums are used with spectral filters to detect Ti, Li, Na and Cd. (see Fig. 10).

3.4. Station 3

The third station had only one single Sony Alpha 7sIII camera mounted with a 30 mm lens. This system is run as a static camera without tracking so that no operator is required. The camera recording is started before the actual entry and stopped after the observation ends.

3.5. Station 4

At station 4, a Nikon Z8 camera with a 300 mm focal length lens is used together with three Allied Vision Alvium cameras: One for tracking, one with a filter for lithium detection (670 nm, 10 nm FWHM) and one with a grating, just in case the emission is bright enough to be spectrally detectable. With the lithium detection, a redundancy is realized with station 2. The grating with 300 lines/mm is combined with 630 nm long-pass filter. Since the filters used in station 1 through 3 might observe two different elements, this grating is intended to help resolve this issue if happened to occur. Fig. 11 shows this setup.

3.6. Window station 5

This station is run by CUB. It consists in a mirror-less Nikon Z6II camera with a Sigma 50 mm lens and a 500 nm long-pass filter. An mp4 video is stored on an internal SD card. The station is combined with an Alvium 1800 U-130 VSWIR camera for short wave infrared (SWIR) detection. Tracking is realized manually on a small tripod, the orientation of the system is manually read out using an I-phone angle measure (*Physics Toolbox* app). Fig. 12 shows the setup, Note, the bubble level on top for an indication of the orientation. The I-phone is not connected in this view

3.7. Window station 6

This station is run by CUB. Two cameras are mounted without any tracking. An Allied Vision Alvium 1800 U-2460 with an $f = 12$ mm lens with a 500 l/mm grating. An additional 500 nm long-pass filter is mounted to suppress daylight. Furthermore, a DMK33UX183 camera is deployed with a Tamron $f = 16$ mm lens and a 770 nm filter to measure potassium (K). Fig. 13 shows the setup

3.8. Ground station

CUB additionally setup a ground observation station. Although the final predictions result in an azimuth of only 5 deg above the horizon, the station is nevertheless setup. Due to the fact that more than half of Easter island is a access controlled natural park requiring a ranger, a location had to be found with simple access which was possible further north on the west coast. A Sony Alpha 7III with a $f = 28$ mm lens and a Panasonic Lumix DC-S5IIX are used. Fig. 14 shows the setup. The cameras are adjusted to look towards the expected entry, which is very low above the horizon. Furthermore, the cloud and rain situation was not promising.

Table 2
Event protocol.

Event No.	Time, UTC	Predicted Distance, km
1	18:47:10.72	917
2	18:47:12.55	900
3	18:47:15.15	870
4	18:47:16.30	860

4. Results

The overall flight mission was executed as planned. After take-off from Easter Island, the location was reached within 1.5 h. Fig. 15 shows the actually flown GPS data overlaid on the pre-flight definition. The maneuver is perfectly aligned with predictions concerning the ground location. The actual aircraft attitude cannot be judged with this plot. Fig. 16 shows the view angles out of the window together with the predictions (see Fig. 6). The two curves are the data read out from the GPS recorder and from the onboard IMU information. The difference is small and might be attributed to the difference between true heading and position over ground. Most importantly, the cameras were viewing almost exactly to where it was planned, i.e. the main break-up location at 18:47:08 UTC at a predicted flight altitude of the spacecraft of around 78 km is well within the field of view. Out of the 26 instruments, 10 detected successfully the spacecraft satellite. Fig. 17 shows the time interval the instruments detected the re-entry. The pre-flight assumptions are given as well. Here, only a schematic approach was feasible since no detailed prediction of the re-entry radiation was feasible. The assumptions from pre-flight are met with the actual observation. The pre-flight assumptions were more optimistic since it had to be considered all potential eventualities, but it is clearly seen that the species detected align with their appearance in the prediction sketch.

During the actual observation, the capsule was not found on the respective screens. The object was also not seen from the cockpit by naked eye. Intuitively, the experimenters followed the predicted view angles (see Fig. 6). This resulted in detectability in post-processing.

Station 1, 3, and 6 did not detect the capsule above the background light. First detection was found in the SWIR imaging system of Station 2. Since it was not seen in the tracking cameras during the actual observation, the anticipated signal amplitude is lower in the real flight. Further analysis of melting and evaporating systems are intended to solve the predictability of the signal intensity.

The detection of the elements K, Li and Al are intended to further derive the fragmentation sequence. It has been shown in ground testing, that the appearance of Li and K is an indicator for a soon to occur break-up of a structure eventually showed by actual Al emission [18].

Fig. 18 shows 4 frames with a peak of flares observed in the camera with the Lithium filter on Station 4. These flares were found post-mission. The first and strongest flare is occurring at 18:47:11 UTC followed by a stronger signal around 18:47:13 UTC. The exact times, referenced to the aluminum-filtered camera, are provided in Table 2. Integrating the intensity values of these flares by summarizing the corresponding pixel data results in a plot as seen in Fig. 19. It shows the normalized photometric light curves from four cameras at station 2, equipped with filters for the emission of aluminum, lithium, sodium and cadmium. In total, four intensity peaks are identified.

The peaks occur almost simultaneously across all cameras. Minor time differences between the instruments are likely due to uncertainties introduced during the frame-saving process. However, these differences may also have a physical meaning.

Comparing these four events with the fragment development in Fig. 4, these flares seem to occur after the first break-up. The main break-up of the Cluster satellite seems to have occurred in these first 10 s after 18:47:10 UT. Compared to the number of fragments as plotted in Fig. 4, the observed flares seem to be detected early in the re-entry.

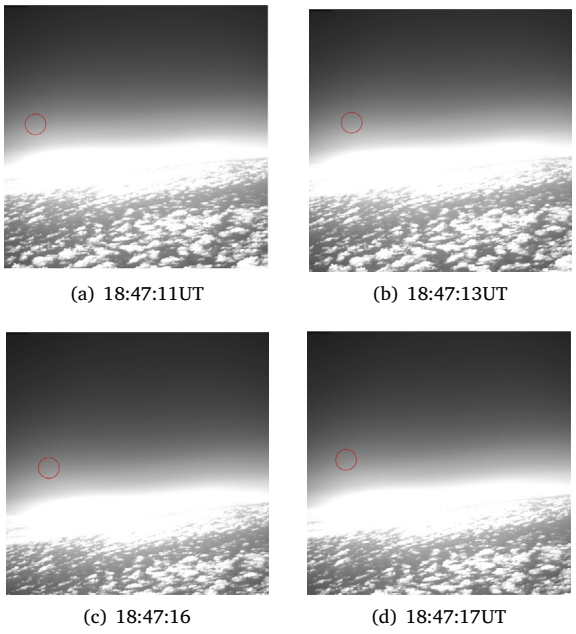

(a) 18:47:11UT (b) 18:47:13UT

(c) 18:47:16 (d) 18:47:17UT

Fig. 18. Raw Images of four observed Lithium signals. It is a tiny dot in the center of the red circle.

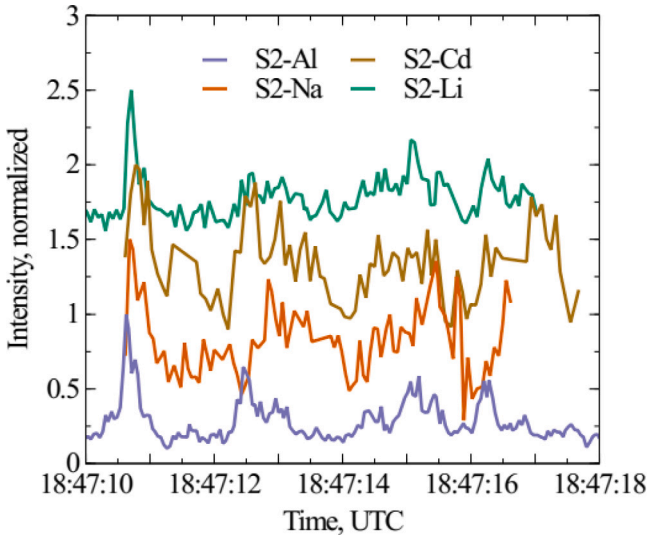

Fig. 19. Normalized photometric lightcurves of four element filtered instruments.

A calibration was performed one day after the mission at Rarotonga International Airport on Cook Islands during night to determine absolute intensity values. For this purpose, a calibration lamp was positioned at a distance of 100 m from the aircraft. A calibration coefficient

$$K_i = \frac{\int_{\lambda_1}^{\lambda_2} L_{CL} \cdot \tau_{filter,i}\, d\lambda \cdot \Omega_{d-l}}{counts \cdot t_e} \tag{1}$$

was determined for each instrument. The spectral radiance of the calibration lamp L_{CL} is multiplied by the spectral transmissivity profile $\tau_{filter,i}$ of the respective filter and integrated over its bandwidth. Multiplication by the solid angle Ω_{d-l} covered by the detector relative to the calibration lamp yields the irradiance detected by the instrument. The calibration coefficient is then obtained by dividing this detected irradiance by the measured counts and the exposure time t_e. Dark

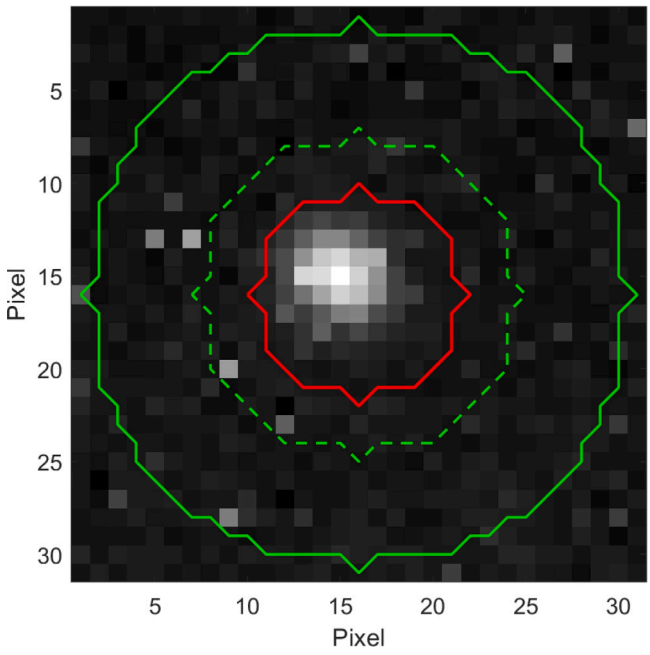

Fig. 20. Example frame from the near-infrared camera at station 2, equipped with the aluminum bandpass filter and the aperture, used for background subtraction and irradiance determination.

frames recorded with identical exposure time were subtracted from the calibration frames. Since the signal from the calibration lamp is spread over multiple pixels, all counts were summed. The aperture and gain were kept identical to those used during the mission. The resulting calibration factor is then applied to determine the irradiance for each camera.

Fig. 20 shows an example frame recorded during the mission. The background signal was obtained by averaging the pixel counts inside the green mask and subtracted from the frame. The intensity was then calculated by summing all pixel counts inside the red circle and multiplying by the corresponding calibration coefficient and exposure time.

Fig. 21 shows the calibrated irradiance for the four instruments mentioned above, with the aluminum signal being the strongest. Also the lithium signal is 1–2 magnitudes higher compared to sodium and cadmium. The intensity recorded by the cameras observing cadmium and sodium drops significantly three times, though the reason for this remains unknown.

Since all peaks occur at the same instant in time across the investigated instruments, the signal might not be attributed to the respective species, but to the continuum radiation of the spacecraft. A blackbody temperature is therefore derived from the data to check whether the signals contain line emission or purely blackbody radiation. The blackbody irradiance of the satellite at the aircraft was approximated using Planck's law:

$$E_{Sat} = \epsilon \cdot \frac{A_{proj}}{r^2} \cdot \int_{\lambda_1}^{\lambda_2} \frac{2\pi hc^2}{\lambda^5 (e^{\frac{hc}{\lambda kT}}) - 1} d\lambda \tag{2}$$

with λ_1 and λ_2 set by the corresponding bandpass filter. A theoretical blackbody temperature was then obtained from this relation. An emissivity of $\epsilon = 1$ was assumed as a conservative first estimate. The average distance between aircraft and satellite was taken as $r = 880$ km. The projected satellite area was approximated as $A_{proj} = 3\,\mathrm{m}^2$. The results are depicted in Fig. 22. The derived temperatures for lithium and aluminum differ strongly from those of cadmium and sodium and are unrealistically high. It is thus concluded that the lithium and aluminum signals also line emissions and thus shown flares are physically meaningful.

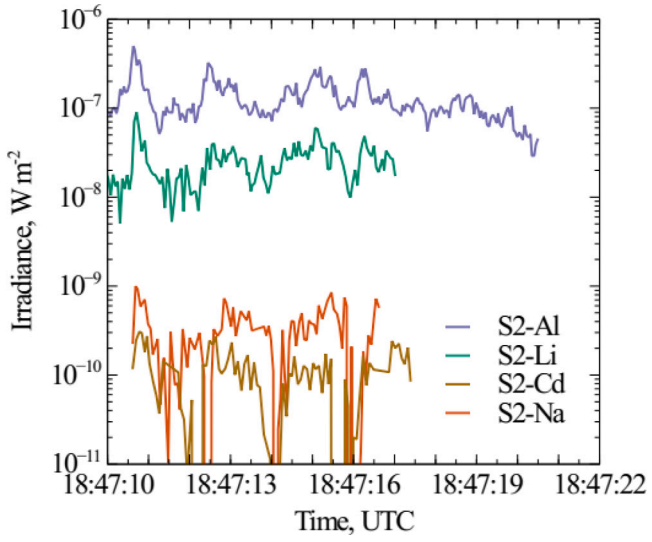

Fig. 21. Calibrated intensities of four element filtered instruments.

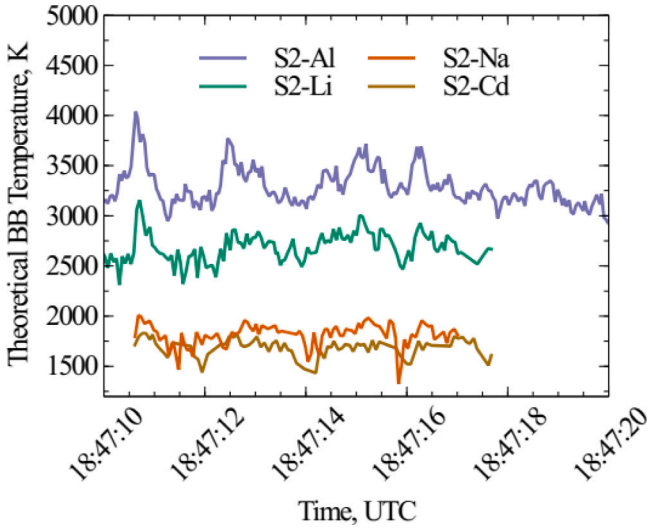

Fig. 22. Theoretical black body temperature according to filtered cameras.

The sequence of flares during the first 30 s of the observation shows that the main fragmentation appears as expected, however, followed by some minor flares with further break-up of the structure. Thus, it is concluded that the Cluster satellite fragmented with a main break-up and the subsequent fragmentation leads to small fragments, the radiation of which is not measurable with the daylight observation constraints and the available camera systems.

5. Summary

The paper describes the design and execution of the airborne re-entry observation mission of the Cluster-II *Salsa* re-entry. It is shown how predictions of orbital state of the satellite, re-entry prediction tools and pre-flight calculations for the aircraft's flight path have to come precisely together in order to successfully observe an object. The particular challenges of this mission being a daytime entry are described. The observation mission concludes recorded data for 10 out of the 26 instruments. The duration of the observation was shorter than predicted. The fragment cloud was not bright enough to be detected during the daytime entry observation.

CRediT authorship contribution statement

Stefan Loehle: Writing – original draft, Visualization, Methodology, Investigation, Data curation, Conceptualization. **Fabian Zander:** Writing – review & editing, Visualization, Methodology, Investigation, Data curation, Conceptualization. **Patrik Kaerraeng:** Writing – review & editing, Software, Investigation, Data curation. **Tobias Lips:** Writing – review & editing, Software, Methodology, Conceptualization. **Gerard Armstrong:** Writing – review & editing, Software, Investigation, Data curation. **Byrenn Birch:** Writing – review & editing, Software, Methodology, Investigation, Data curation, Conceptualization. **Ranjith Ravichandran:** Writing – review & editing, Visualization, Methodology, Investigation, Data curation. **Clemens Mueller:** Writing – original draft, Visualization, Methodology, Investigation, Data curation. **Juraj Toth:** Writing – review & editing, Data curation. **Tomasz Paulech:** Writing – review & editing, Data curation. **Jiri Silha:** Writing – review & editing, Funding acquisition. **Beatriz Jilete:** Writing – review & editing, Project administration, Methodology, Data curation, Conceptualization. **Stijn Lemmens:** Writing – review & editing, Project administration, Conceptualization.

Declaration of competing interest

The authors declare that they have no known competing financial interests or personal relationships that could have appeared to influence the work reported in this paper.

Acknowledgments

The authors thank the FalconAir team for the incredible support and endurance to answer every request of the researchers, our pilots who brought us safely to the most remote airport worldwide and last but not least the workshop teams in the different countries for their fast solution focused support. This work is funded through the European Space Agency contract No. 4000145029/24/D/MRP.

References

[1] F. Zander, S. Löhle, A review of airborne observations for space debris re-entry break-up and dispersion measurements, CEAS Space J. (2025).
[2] ESA Space Debris Mitigation Working Group, in: ESA (Ed.), ESA Space Debris Mitigation Requirements, ESA Space Debris Mitigation Working Group ESSB-ST-U-007, 2023.
[3] L. Innocenti, ESA clean space initiative, 2013.
[4] S. Loehle, R. Wernitz, G. Herdrich, M. Fertig, H.-P. Röser, H. Ritter, Airborne re-entry observation experiment SLIT: UV spectroscopy during stardust and ATV1 re-entry, CEAS Space J. 1 (1) (2010).
[5] J.B. Snively, M.J. Taylor, P. Jenniskens, Airborne imaging and NIR spectroscopy of the ESA ATV spacecraft re-entry: Instrument design and preliminary data description, Int. J. Remote Sens. 32 (11) (2011) 3019–3027.
[6] S. Loehle, P. Jenniskens, T. Lips, B. Bastida-Virgili, J. Albers, F. Zander, H. Krag, J.H. Grinstead, J. Bacon, Preparations of the airborne ATV-5 re-entry observation campaign, in: 12th International Planetary Probe Workshop, NASA, Pasadena, CA, USA, 2015.
[7] P. Jenniskens, J. Albers, M. Koop, M. Odeh, K. Al-Noimy, K. Al-Remeithi, K. Al Hasmi, R.F. Dantowitz, F. Gasdia, S. Loehle, F. Zander, T. Hermann, D. Farnocchia, S.R. Chesley, P.W. Chodas, R.S. Park, J.D. Giorgini, W.J. Gray, D.K. Robertson, T. Lips, Airborne observations of an asteroid entry for high fidelity modeling: Space debris object WT1190F, in: 54th AIAA Aerospace Sciences Meeting, in: AIAA SciTech Forum, AIAA American Institute of Aeronautics and Astronautics, Reston, VA, USA, 2016.
[8] T. Watson, Falling space debris traced to 1998 lunar mission, Nature (2016).
[9] S. Loehle, M. Eberhart, F. Zander, A. Meindl, R. Rudawska, D. Koschny, J. Zender, R. Dantowitz, P. Jenniskens, Extension of the plasma radiation database PARADE for the analysis of meteor spectra, Meteorit. Planet. Sci. (2021).
[10] P. Jenniskens, P. Wercinski, J. Olejniczak, G.A. Raiche, D.A. Kontinos, G.A. Allen, P.N. Desai, D. Revelle, J. Hatton, R.L. Baker, R.W. Russel, M. Taylor, F. Rietmeijer, Preparing for the hyperseed MAC: An observing campaign to monitor the entry of the genesis sample return capsule, Earth Moon Planets (95) (2004).
[11] P. Jenniskens, Observations of the stardust sample return capsule entry with a slitless echelle spectrograph, J. Spacecrafts Rocket. 47 (5) (2010).

[12] J.H. Grinstead, P. Jenniskens, A. Cassell, J. Albers, M.W. Winter, Airborne observation of the hayabusa sample return capsule re-entry, in: 42nd AIAA Thermophysics Conference, AIAA American Institute of Aeronautics and Astronautics, Reston, VA, USA, 2011.
[13] S. Loehle, P. Jenniskens, High resolution spectroscopy of the Hayabusa re-entry using a Fabry-Perot interferometer, J. Spacecrafts Rocket. 51 (6) (2014) 1986–1993.
[14] F. Zander, D. Buttsworth, B. Birch, A. Payne, Planning and implementation of the Australian airborne observation of Hayabusa2, in: AIAA AVIATION 2022 Forum, AIAA American Institute of Aeronautics and Astronautics, Reston, Virginia, 2022.
[15] C. Mueller, D. Leiser, S. Loehle, S. Fasoulas, Reentry break-up analysis of materials under transient thermomechanical loads in plasma wind tunnels, in: AIAA Aviation Forum, AIAA American Institute of Aeronautics and Astronautics, Reston, Virginia, 2024.
[16] T. Lips, B. Fritsche, A comparison of commonly used re-entry analysis tools, Acta Astronaut. 57 (2–8) (2005) 312–323.
[17] L. Lees, Laminar heat transfer over blunt-nosed bodies at hypersonic flight speeds, J. Jet Propuls. 26 (4) (1956) 259–269.
[18] D. Leiser, S. Loehle, S. Fasoulas, Spectral features for re-entry break-up event identification, J. Spacecr. Rockets 59 (5) (2022) 1496–1506.